MESSENGER detection of electron-induced X-ray fluorescence from Mercury's surface

Richard D. Starr,[1] David Schriver,[2] Larry R. Nittler,[3] Shoshana Z. Weider,[3] Paul K. Byrne,[3] George C. Ho,[4] Edgar A. Rhodes,[4] Charles E. Schlemm II,[4] Sean C. Solomon,[3,5] and Pavel M. Trávníček[6]

Received 2 May 2012; revised 27 June 2012; accepted 28 June 2012; published 16 August 2012.

[1] The X-Ray Spectrometer (XRS) on the MESSENGER spacecraft measures elemental abundances on the surface of Mercury by detecting fluorescent X-ray emissions induced on the planet's surface by the incident solar X-ray flux. The XRS began orbital observations on 23 March 2011 and has observed X-ray fluorescence (XRF) from the surface of the planet whenever a sunlit portion of Mercury has been within the XRS field of view. Solar flares are generally required to provide sufficient signal to detect elements that fluoresce at energies above ~2 keV, but XRF up to the calcium line (3.69 keV) has been detected from Mercury's surface at times when the XRS field of view included only unlit portions of the planet. Many such events have been detected and are identified as electron-induced X-ray emission produced by the interaction of ~1–10 keV electrons with Mercury's surface. Electrons in this energy range were detected by the XRS during the three Mercury flybys and have also been observed regularly in orbit about Mercury. Knowledge of the energy spectrum of the electrons precipitating at the planet's surface makes it possible to infer surface composition from the measured fluorescent spectra, providing additional measurement opportunities for the XRS. Abundance results for Mg, Al, and Si are in good agreement with those derived from solar-induced XRF data, providing independent validation of the analysis methodologies. Derived S and Ca abundances are somewhat higher than derived from the solar-induced fluorescence data, possibly reflecting incomplete knowledge of the energy spectra of electrons impacting the planet.

Citation: Starr, R. D., D. Schriver, L. R. Nittler, S. Z. Weider, P. K. Byrne, G. C. Ho, E. A. Rhodes, C. E. Schlemm II, S. C. Solomon, and P. M. Trávníček (2012), MESSENGER detection of electron-induced X-ray fluorescence from Mercury's surface, *J. Geophys. Res.*, *117*, E00L02, doi:10.1029/2012JE004118.

1. Introduction

[2] X-ray emission from solar system bodies has been observed for decades. Atoms near the surface of planetary bodies with no atmosphere may be excited by solar X-rays, solar wind particles (primarily electrons), and ions, producing line emission and bremsstrahlung. The first planetary X-ray fluorescence (XRF) detections were made by Luna 12 in 1968 [*Adler et al.*, 1973] and then by the X-ray spectrometers on Apollo 15 and 16 [*Adler et al.*, 1972a, 1972b]. X-rays from Jupiter and the Galilean satellites, produced by particles (mostly heavy ions) trapped in the Jovian magnetosphere, were originally detected by the Einstein X-Ray Observatory [*Metzger et al.*, 1983]. X-ray emission from comets was first reported in 1996 when the ROSAT satellite observed comet Hyakutake [*Lisse et al.*, 1996]. The atmospheres of Earth, Venus, and Mars have also been studied in the X-ray energy regime [e.g., *Fink et al.*, 1988; *Cravens and Maurellis*, 2001]. The focus of most of these studies has been to identify and better understand the interaction of the several excitation sources (solar X-rays, heavy ions, magnetospheric electrons, and ions) that give rise to these X-ray emissions. (For a summary of the many observations of X-ray emissions from solar system bodies, see, for example, *Bhardwaj et al.* [2007] and references therein.) In cases for which the spectrum of exciting particles is known and the physics of interactions in materials is well understood, the resulting X-ray emissions may provide

[1]Physics Department, Catholic University of America, Washington, D. C., USA.
[2]Department of Physics and Astronomy and Institute of Geophysics and Planetary Physics, University of California, Los Angeles, California, USA.
[3]Department of Terrestrial Magnetism, Carnegie Institution of Washington, Washington, D. C., USA.
[4]Johns Hopkins University Applied Physics Laboratory, Laurel, Maryland, USA.
[5]Lamont-Doherty Earth Observatory, Columbia University, Palisades, New York, USA.
[6]Space Sciences Laboratory, University of California, Berkeley, California, USA.

Corresponding author: R. D. Starr, Physics Department, Catholic University of America, Washington, DC 20064, USA. (richard.d.starr@nasa.gov)

information on the composition of the target material. Such is the case with solar-induced X-ray fluorescence, by which measurements of X-ray emissions from planetary surfaces have been used to infer surface elemental abundances. Orbiting spacecraft at the Moon [*Adler et al.*, 1972a,1972b; *Narendranath et al.*, 2011; *Weider et al.*, 2012], the asteroids 433 Eros and 25143 Itokawa [*Trombka et al.*, 2000; *Okada et al.*, 2006], and most recently Mercury [*Nittler et al.*, 2011] have provided details of surface composition for a number of important rock-forming elements.

[3] The interaction of low-energy electrons (<100 keV) with materials is also well understood. Indeed, electron-induced X-ray fluorescence is a well-established laboratory technique for measuring the composition of materials [e.g., *Goldstein et al.*, 2003]. On a planetary scale, electron-induced X-ray fluorescence has been observed, but the phenomenon has not heretofore been used as a tool for planetary geochemistry because of uncertainties in the electron excitation spectrum.

[4] Electron-induced X-ray emission has been observed by the SELENE SOL-C X-Ray Spectrometer from lunar orbit [*Okada et al.*, 2010]. X-ray fluorescence during lunar nighttime was detected from the standard sample plate over a period of 30 min. Line emission up to Fe (6.4 keV) was observed. *Burbine et al.* [2005] studied the possibility of detecting electron-induced X-ray fluorescence from the nightside of Mercury. Given some reasonable assumptions about electron energy and flux intensity based on Mariner 10 observations, they concluded that such measurements are possible and that X-ray emission at the lines for Mg, Al, and Si may be comparable to what would be measured from flares on the sunlit portion of the planet.

[5] Prior to the MErcury Surface, Space ENvironment, GEochemistry, and Ranging (MESSENGER) mission, little was known about the makeup of the charged particles in Mercury's magnetosphere. Mariner 10 detected high-energy particles in the magnetosphere of Mercury that were seen in a series of bursts, suggesting that they were not stable trapped particles but were most likely accelerated by the planet's magnetotail or magnetosheath [*Simpson et al.*, 1974]. Evidence for low-energy electrons around Mercury was provided by the MESSENGER X-Ray Spectrometer (XRS) during the three MESSENGER flybys of Mercury and later confirmed by the spacecraft's Energetic Particle Spectrometer (EPS) following orbit insertion [*Ho et al.*, 2011a, 2011b].

[6] Since MESSENGER entered orbit about Mercury, the spacecraft's XRS has routinely seen the same signature of low-energy (1–10 keV) electrons, generally near periapsis [*Ho et al.*, 2011b]. On the basis both of these observations and models of the process, this quasi-trapped electron (and ion) population forms around the nightside of the planet near the geomagnetic equator at a radial distance of ~1.4 R_M (where R_M is Mercury's radius, or 2440 km) [*Schriver et al.*, 2011b]. Additionally, the XRS has made multiple detections of X-ray fluorescence from the nightside of the planet, the result of these low-energy electrons impinging on the planet's surface. Measurements of both the exciting electron spectrum and the resulting X-ray fluorescence from Mercury's surface provide the MESSENGER XRS with the opportunity to infer surface chemistry through electron-induced XRF.

[7] This work presents results from an analysis of sixteen electron-induced XRF events. Inferred elemental compositions are provided for Mg, Al, S, Ca, Ti, and Fe, and the results reported here are generally in line with those from solar-induced XRF measurements.

2. MESSENGER X-Ray Spectrometer

[8] The X-Ray Spectrometer instrument on MESSENGER is comprised of three identical gas proportional counters (GPCs) that measure X-rays emitted from the surface of Mercury in the 1–10 keV energy range [*Schlemm et al.*, 2007]. The counters each have a 10 cm^2 active area and use both anti-coincidence wires placed around the inner periphery of the tube and pulse-shape discrimination to minimize background, due primarily to galactic cosmic rays (GCRs). Balanced filters, similar to those used on the Apollo 15, 16, and Near Earth Asteroid Rendezvous (NEAR) missions, are used to resolve the lower-energy X-ray lines from Mg, Al, and Si, at 1.254, 1.487, and 1.740 keV, respectively [*Adler et al.*, 1972a,1972b; *Nittler et al.*, 2001]. A thin foil of Mg (4.5 μm) on one detector and of Al (6.3 μm) on another are mounted over the GPC entrance windows [*Schlemm et al.*, 2007]. The third detector has no filter. From the simultaneous analysis of the spectra from all three detectors, the flux of photons in the three lines can be uniquely determined. The energy resolution of the gas counters is sufficient to resolve the higher-energy lines from S (2.307 keV), Ca (3.690 keV), Ti (4.508 keV), and Fe (6.404 keV). A small (0.03 mm^2) Si-PIN detector is used as a solar monitor, because the Sun is the primary source of the planetary X-ray fluorescence and knowledge of the highly variable flux is required for accurate modeling. The XRS is similar to the X-ray spectrometers flown on the Apollo 15 and 16 missions [*Adler and Trombka*, 1977] and to the NEAR X-ray spectrometer [*Starr et al.*, 2000]. The most important improvement in the MESSENGER XRS over the previous instruments is the quality of the background rejection in the gas proportional counters. On Apollo, background rejection was ~90%, but measurements were made only in the 1–2 keV energy region [*Adler et al.*, 1972a, 1972b]. On NEAR, background rejection was used only above 3 keV, which limited the quality of quiet-Sun measurements [*Nittler et al.*, 2001]. On MESSENGER, the background rejection is ~90% over the entire energy range of interest, allowing measurements of Mg, Al, and Si line emissions in minutes rather than days, even during quiet solar conditions [*Solomon et al.*, 2001].

[9] The field of view (FOV) of the XRS is 12°, and even at apoapsis Mercury can fill the FOV. The highly eccentric orbit of the MESSENGER spacecraft has a large impact on the spatial resolution of the XRS. At periapsis (at high northern latitudes) the spatial resolution may be as fine as ~60 km (for measurements that are not photon limited), whereas at apoapsis the resolution is several thousand kilometers [*Schlemm et al.*, 2007].

3. Electrons at Mercury

3.1. Electron Energies

[10] Prior to the MESSENGER flybys of Mercury, the only spacecraft to visit the innermost planet of our Solar

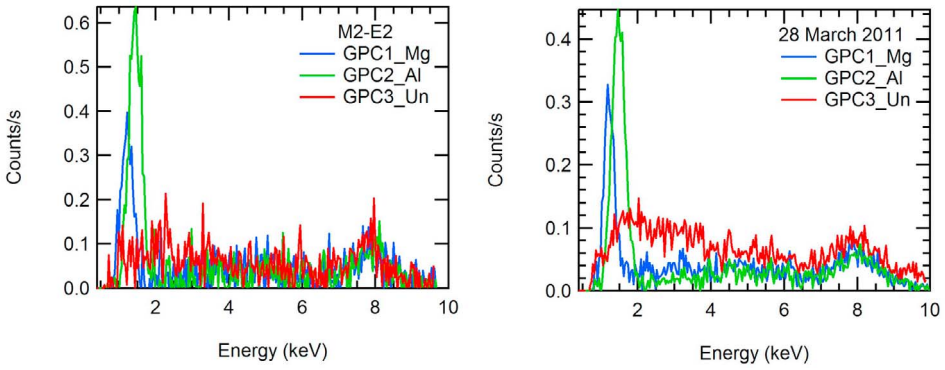

Figure 1. Typical spectra measured by the three XRS gas proportional counters (GPCs) from the interaction of ~1–10 keV electrons with the Mg-filtered (blue), Al-filtered (green), and unfiltered (red) GPC. Fluorescence of the Mg and Al filters at 1.25 and 1.49 keV, respectively, is seen in the filtered detectors. All three GPCs show evidence of the 8.05 keV Cu line produced by electrons impinging on the Be–Cu collimator. (left) The M2-E2 event [*Ho et al.*, 2011a]. (right) The event of 28 March 2011.

System was Mariner 10, which flew by Mercury twice in 1974 and once in 1975. The *Simpson et al.* [1974] interpretation of Mariner 10 measurements of energetic particles has been questioned by several authors (see, for example, the summary by *Wurz and Blomberg* [2001]). In particular, the very high electron energies, in excess of 0.5 MeV, suggested by *Simpson et al.* are difficult to explain within the context of Mercury's relatively small magnetosphere [*Russell et al.*, 1988].

[11] MESSENGER flyby and orbital observations have provided new measurements of Mercury's magnetic field and energetic particle population [*Anderson et al.*, 2011; *Ho et al.*, 2011a, 2011b]. The first indirect detection of Mercury's energetic electrons was made by MESSENGER's XRS during each of the three flybys. The XRS measured several count-rate spikes within minutes of closest approach (both before and after) whose signatures clearly identify their origin as electrons (~1–10 keV) interacting with the XRS detector material [*Ho et al.*, 2011a]. Electron-induced fluorescence and bremsstrahlung produced by electrons impinging on the XRS Mg and Al filters, Be windows, and Be-Cu collimator are evident in the XRS gas proportional counters, as seen in Figure 1 (left) for the second of two events detected during the second Mercury flyby (M2-E2). However, no corresponding signal was observed by the EPS for these events either due to differences in instrument FOV or to a drop off in electron flux above the ~35 keV energy threshold of the EPS.

[12] Since the beginning of orbital operations at Mercury, similar electron events have been detected by XRS during almost every orbit. One such event from 28 March 2011 is shown in Figure 1 (right). These electron events last from minutes to tens of minutes and are almost always observed close to periapsis. Following orbit insertion, the EPS has also made definitive electron detections [*Ho et al.*, 2011b]. Although energies may exceed 200 keV, a spectral cutoff near 100 keV is frequently observed. The picture of Mercury's energetic electron population that is now coming into focus is that of a lower energy distribution than first suggested by *Simpson et al.* [1974], marginally constrained by Mercury's weak magnetic field [*Ho et al.*, 2011b; *Schriver et al.*, 2011b]. An electron transport model suggests that a large percentage of these quasi-trapped electrons do not complete even a single drift orbit about Mercury before impacting the surface or being lost to the downstream solar wind after colliding with the magnetopause boundary layer [*Schriver et al.*, 2011a].

3.2. Electron Spectra

[13] The XRS flyby detection of electrons described by *Ho et al.* [2011a] offered a first glimpse of Mercury's electron spectral distribution. Modeling of the XRS measurements with a kappa-function energy distribution [*Christon*, 1987] provided a good match to the measurements. The inferred electron spectrum from *Ho et al.* [2011a] for the M2-E2 event is shown in Figure 2 (left).

[14] Since MESSENGER entered orbit about Mercury, the EPS has made numerous detections of electron events above its low-energy cutoff of ~35 keV. XRS is most sensitive to electron energies below ~10 keV, but the modeled electron spectrum may be extended to 100 keV, as illustrated in Figure 2. In Figure 2 (right), the modeled XRS electron spectrum is compared with a typical EPS detection from 28 March 2011. The similarity of the M2-E2 and the 28 March 2011 events, shown in Figure 1, illustrates the repeatability of these events and suggests that the electron model for M2-E2 is valid as well for the events observed since orbit insertion. The similarity between the slopes of the EPS measurement and the XRS model seen in Figure 2 provides further validation of the XRS modeling.

3.3. Electron-Induced X-Ray Fluorescence

[15] Since MESSENGER entered into orbit about Mercury the XRS has observed more than 30 instances of electron-induced X-ray emission from the surface of Mercury. Many of these detections are combined with solar-induced fluorescence. The electron-induced emission is generally of the same magnitude as quiet-Sun fluorescence, which

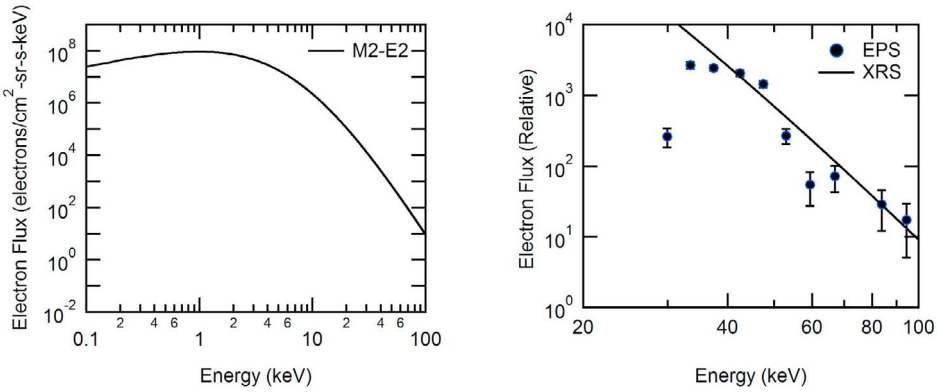

Figure 2. (left) Electron flux inferred from XRS measurements during MESSENGER's second Mercury flyby [*Ho et al.*, 2011a]. (right) The same modeled XRS electron flux (black line) is compared with an EPS spectrum from 28 March 2011.

complicates the analysis. Sixteen of these events have little or no solar contribution, and these, listed in Table 1, are the subject of this investigation. The XRS footprints for these events are overlaid on an image mosaic of the planet in Figure 3. These footprints indicate the full instrument FOV on the surface of the planet for these measurements. Unlike the solar measurements, for which the sunlit portion of the FOV is well defined, we cannot say where within the footprint the electron-induced emissions originate. The X-ray emissions may fill all of the footprint or any part of it.

[16] Two example electron X-ray emission events, a 450-s integration on 6 May 2011 (number 2, Figure 4, left), and a 300-s integration on 13 August 2011 (number 5, Figure 4, right) are shown in Figure 4. The two events are similar, with both displaying XRF signals up to the energy of the Ca line at 3.69 keV. There is a smooth continuum above the Ca line, with little evidence for emission from elements such as Ti or Fe that fluoresce at energies above that of Ca.

3.4. Electron Precipitation at Mercury

[17] The electron-induced emission events seen by XRS are likely due to the precipitation of ~1–10 keV electrons onto the surface of Mercury. Figure 5 shows a map, in latitude versus local time (LT), of the energy of precipitating electrons from a transport model that follows the trajectories of electrons in a snapshot of global electric and magnetic fields of Mercury's magnetosphere obtained from a hybrid (i.e., semi-kinetic) simulation [*Trávníček et al.*, 2010; *Schriver et al.*, 2011a]. The precipitation pattern depends on the solar wind interplanetary magnetic field (IMF) direction. Figure 5 shows simulations both for northward-directed IMF and southward-directed IMF. Evident are a number of "hot spots" with precipitation energies of ~1 keV under both solar wind IMF conditions, although for southward IMF the energies are slightly higher. The precipitating fluxes at the hot spots are $\sim 10^9$ cm^{-2}s^{-1} [*Schriver et al.*, 2011a]. Although globally the precipitation energies are about the same, the different precipitation hot spots are generally caused by different sources. The dayside (~12 h LT) high-latitude hot spot is primarily the result of cusp precipitation [*Schriver et al.*, 2011a; *Zurbuchen et al.*, 2011], the afternoon to morning equatorial region the product of low-latitude boundary layer electrons [*Schriver et al.*, 2011a], and the nightside (0–6 and 18–24 h LT) higher-latitude precipitation the result of quasi-trapped electrons [*Schriver et al.*, 2011b; *Korth et al.*, 2011].

[18] The positions in local time of observed XRS fluorescence events are also shown in Figure 5. Although the range of observed events is from just prior to midnight (~22 h LT) to around noon (~12 h LT), the majority of the events (events 3–16 listed in Table 1) occurred in the early morning hours between midnight and about ~4 h LT, and only events 1 and 2 occurred between dawn (~6 h LT) and noon. There is qualitative agreement between the simulated electron precipitation pattern on the nightside–morning region and the XRS fluorescence events, but there is not a 1-to-1 correspondence for each individual event. One possible reason for the lack of full agreement is that the precipitation locations of highly mobile electrons depend strongly on the solar wind parameters, in particular pressure and IMF orientation, as can be seen by comparing the two panels in Figure 5. During most of the events the solar wind IMF was constantly

Table 1. Electron-Induced Fluorescence Events[a]

Event	DOY	Date	UTC Start	Duration (s)	LT Start	LT End
1	123	3 May 2011	16:43:10	900	06:18	12:42
2	126	6 May 2011	02:50:48	450	22:48	13:48
3	140	20 May 2011	09:35:06	240	01:36	03:00
4	175	24 June 2011	11:35:20	1350	00:36	04:12
5	225	13 August 2011	08:49:12	300	02:48	04:12
6	225	13 August 2011	20:50:52	280	02:54	04:18
7	308	4 November 2011	21:09:02	1600	23:00	03:18
8	314	10 November 2011	21:55:33	140	02:24	03:06
9	344	10 December 2011	20:25:10	1200	03:18	05:18
10	345	11 December 2011	20:01:11	1300	02:42	04:42
11	348	14 December 2011	06:58:59	300	23:24	01:42
12	349	15 December 2011	06:46:43	200	23:06	01:06
13	350	16 December 2011	18:13:33	600	21:30	01:30
14	351	17 December 2011	05:16:02	40	01:12	01:36
15	351	17 December 2011	17:03:32	20	00:54	01:18
16	364	30 December 2011	23:25:38	140	23:06	01:06

[a]Notes: DOY is day of the year. UTC is Coordinated Universal Time. LT is local time.

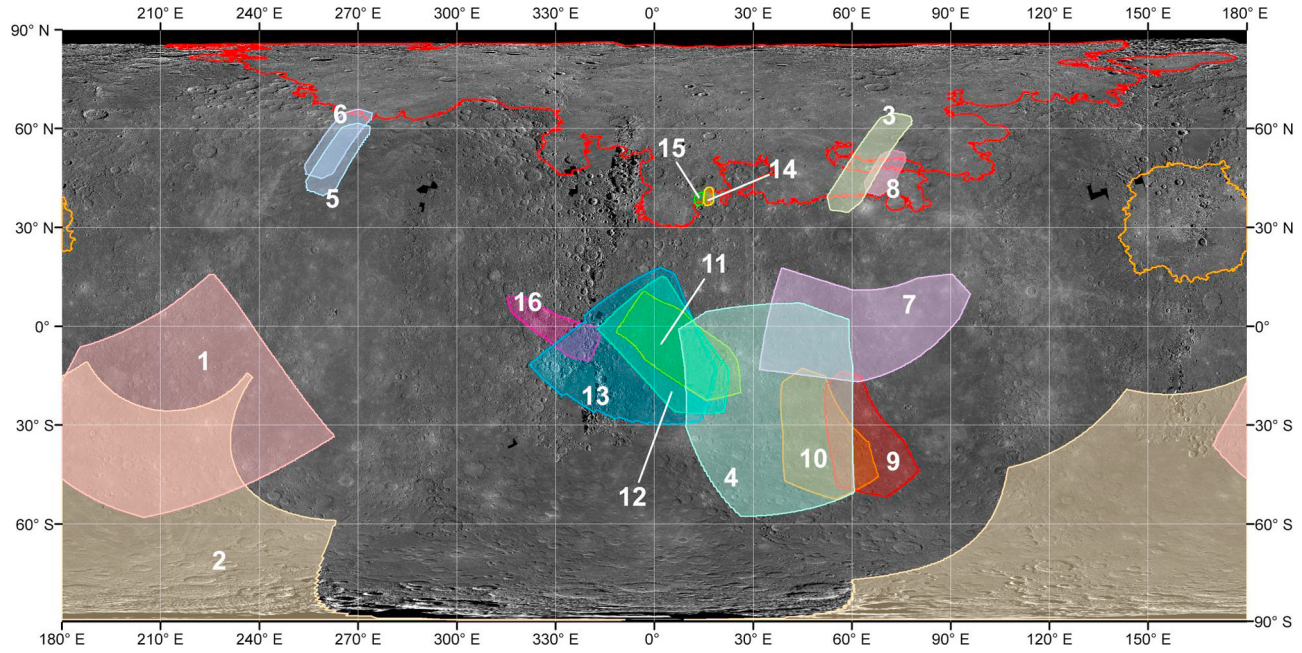

Figure 3. Footprints of the 16 electron-induced fluorescence events superimposed on a Mercury Dual Imaging System (MDIS) mosaic of Mercury. The northern volcanic plains are outlined in red, and the rim of the Caloris basin is traced in orange. The numbering scheme follows that in Table 1.

changing from northward to southward on time scales of minutes or less, which is on the order of the XRS event durations (see Table 1), whereas the simulated results were obtained for a given (constant) configuration of the IMF and Mercury's magnetosphere. Nevertheless, the precipitation energies and locations shown in the Mercury global electron model strongly support that these 1–10 keV precipitating electrons are the cause of the observed XRS fluorescence events.

4. Modeling Procedure

[19] Modeling of these events was accomplished with the Monte Carlo N-Particle Extended (MCNPX) code developed at the Los Alamos National Laboratory [*Pelowitz*, 2005]. The MCNPX model of the GPC detectors has been verified through laboratory measurements and in-flight measurements of astrophysical X-ray sources. In particular, the well-known supernova remnant Cassiopeia-A has been observed by the GPC detectors more than 10 times during the spacecraft's heliocentric trajectory and once during orbit about Mercury to verify instrument operation and to look for changes in detector response. The observed GPC spectra match closely the known X-ray spectrum of Cassiopeia-A when propagated through the modeled response function for each of the detectors, confirming the validity of the model.

[20] *Nittler et al.* [2011, hereafter N11] compared XRS solar-induced XRF results for Mercury's surface to a number

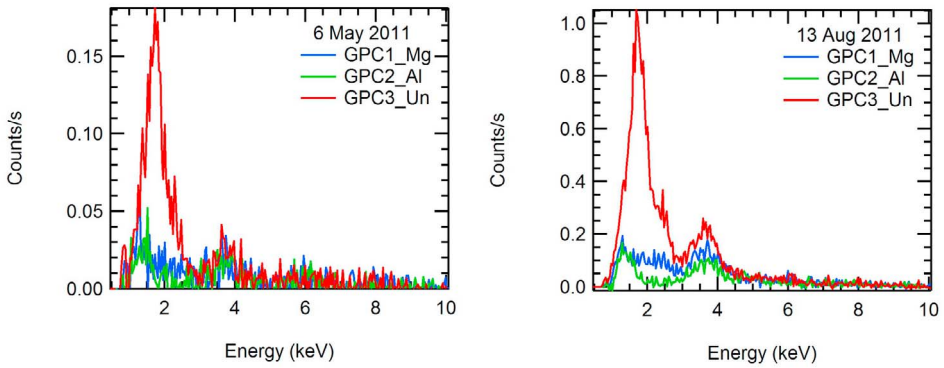

Figure 4. Spectra of two electron-induced X-ray fluorescence events. (left) Event number 2 on 6 May 2011. (right) Event number 5 on 13 August 2011.

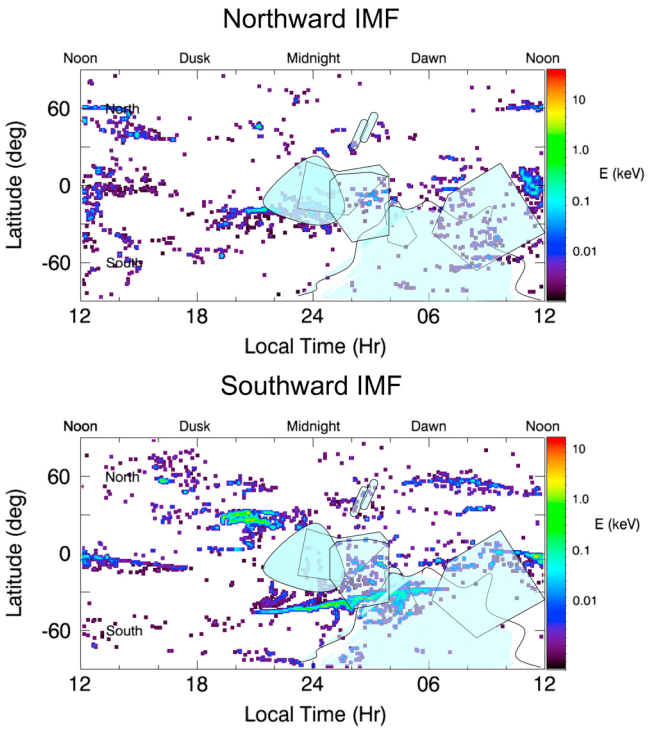

Figure 5. Electron precipitation at the surface of Mercury predicted by global kinetic particle simulations is shown versus latitude and local time and color coded by average energy. The simulation results for (top) a northward oriented IMF and (bottom) a southward oriented IMF. Both results are for low to moderate solar wind dynamic pressure. The light-blue shaded regions show the positions in local time of the observed XRS fluorescence events listed in Table 1.

of different suggested compositions and reported that the enstatite chondrite partial melt composition of *Burbine et al.* [2002, hereafter B02] is a relatively good match to the observations, although it has slightly higher S and Ca than that derived from the XRS spectra (see Table 2 for the B02 composition). With this composition and the modeled electron flux from *Ho et al.* [2011a], the resulting spectrum of electron-induced X-ray emission and bremsstrahlung continuum from Mercury's surface can be modeled.

[21] Example model results based on the M2-E2 electron spectrum and B02 composition are shown in Figure 6 for two events, from 6 May 2011 (number 2) and 14 December 2011 (number 11). The model spectra were scaled to best match the measurements in the unfiltered GPC, which has the best count statistics of the three detectors. The same scaling factor was then applied to the two filtered GPCs. As can be seen in Figure 6, the model reproduces the measurements fairly well. To further constrain the composition, individual element abundances were then varied one at a time to obtain a best match to the data and to estimate statistical uncertainties from the goodness of fit. In the next section, we discuss the composition results for the elements detected by XRS and the variability of the sample set, and we provide an estimate of systematic uncertainties. Abundance values for Mg, Al, S, and Ca are given in Table 3 for all 16 events.

5. Elemental Abundance Results

5.1. Magnesium, Aluminum, and Silicon

[22] The measured elemental abundances for Mg and Al for the 16 events are generally in good agreement with B02. The relatively low B02 value for Al (Table 2) agrees with the N11 measurements, and together with relatively low values for Ca (see below) is indicative of a planet with a low surface abundance of plagioclase feldspar. The Mg abundance, on the other hand, is high and matches those observed in mafic and ultramafic rock types.

[23] N11 and S. Z. Weider et al. (Chemical heterogeneity on Mercury's surface revealed by the MESSENGER X-Ray Spectrometer, submitted to *Journal of Geophysical Research*, 2012) found that the Mg/Si ratio varies over the surface of the planet. In particular, for the northern volcanic plains (NVP) [*Head et al.*, 2011], XRS solar-induced XRF measurements yield, on average, lower values for Mg/Si than elsewhere on the planet (Weider et al., submitted manuscript, 2012). The footprints of two of the electron events, detected on 20 May 2011 (number 3 in Tables 1 and 3) and 10 November 2011 (number 8), are located over the NVP, as shown in Figure 3. The footprints of these two events nearly overlap; that for the 10 November event is smaller and covers less of the northern plains region. These two events are compared with the standard B02 model (Mg/Si=0.45) and with a model in which the Mg is reduced to 6.3 wt% (Mg/Si = 0.25) in Figure 7. The spectrum for the 20 May event is better described by this lower-Mg model, but the standard model better matches that for the 10 November event.

[24] The difference between the 20 May and 10 November events may be partly explained by the uncertainty in the location within the footprints at which the two surface emissions originate. If most of the emissions for the 10 November event originated in the region outside the NVP, for instance, we might expect a higher Mg abundance. However, given the geometry of the footprints, it seems more likely that the two measurements reflect a real difference in Mg abundance within the NVP, despite the close proximity of the footprints.

[25] It is also worth noting that whereas the solar flare analysis of Weider et al. (submitted manuscript, 2012) shows generally lower Mg abundances in the NVP than in

Table 2. Enstatite Chondrite Partial Melt Composition of *Burbine et al.* [2002]

Element	Weight %
O	46.9
Na	0.00
Mg	11.5
Al	7.15
Si	25.7
K	0.00
Ca	8.36
Ti	0.12
Cr	0.00
Mn	0.09
Fe	0.19
S	4.00

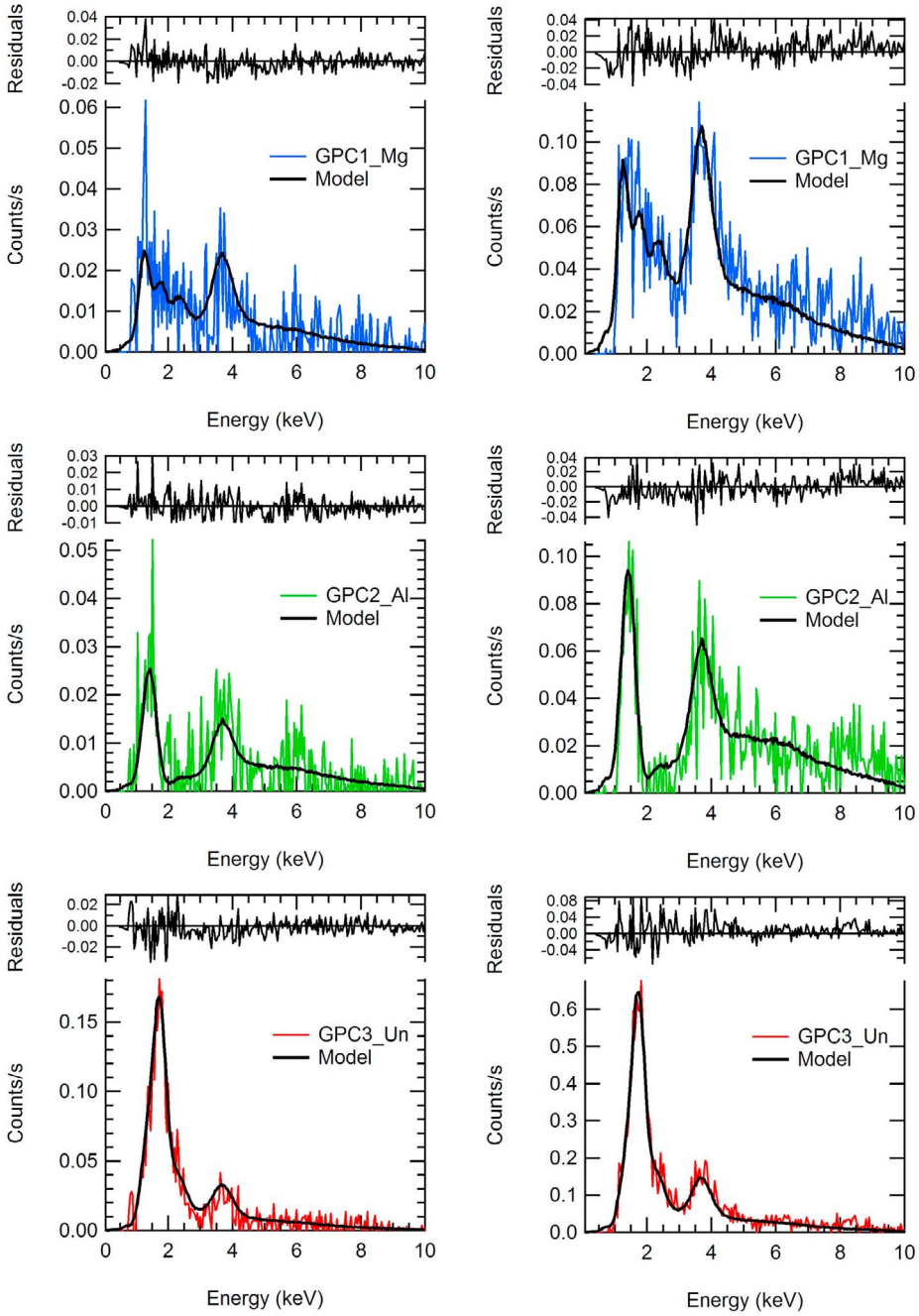

Figure 6. Model fits to spectra from two electron-induced fluorescence events on (left) 6 May 2011 (number 2) and (right) 14 December 2011 (number 11). The model uses the M2-E2 electron distribution and the B02 composition. Model results are scaled to match the measurements. Residuals in this figure and all following figures are the difference between the measured and modeled spectra in counts/s.

Table 3. Mercury Surface Compositions (wt%) Inferred From Electron-Induced Fluorescence Events[a]

Event	DOY	Date	Mg	Al	S	Ca
B02	-	-	**11.5**	**7.2**	**4.0**	**8.4**
1	123	3 May 2011	9.8 ± 8.9	8.5 ± 4.6	4.1 ± 1.3	9.2 ± 3.6
2	126	6 May 2011	14.3 ± 6.8	7.9 ± 2.3	3.9 ± 1.0	5.6 ± 2.8
3	140	20 May 2011	6.3 ± 1.1	5.8 ± 0.9	3.9 ± 0.4	9.5 ± 1.6
4	175	24 June 2011	8.5 ± 5.7	4.8 ± 1.4	4.0 ± 0.7	7.6 ± 1.9
5	225	13 August 2011	11.5 ± 1.3	4.9 ± 0.6	6.7 ± 0.9	8.7 ± 1.2
6	225	13 August 2011	11.8 ± 2.9	5.6 ± 1.3	4.0 ± 0.7	4.7 ± 1.3
7	308	4 November 2011	8.2 ± 1.0	4.9 ± 0.5	2.2 ± 0.2	9.2 ± 1.0
8	314	10 November 2011	11.0 ± 3.8	6.4 ± 1.9	4.5 ± 0.9	6.7 ± 2.7
9	344	10 December 2011	12.8 ± 4.6	7.0 ± 1.5	4.0 ± 0.6	4.4 ± 1.1
10	345	11 December 2011	12.2 ± 1.6	7.8 ± 1.0	4.3 ± 0.4	9.0 ± 0.8
11	348	14 December 2011	11.3 ± 3.4	6.6 ± 1.2	4.3 ± 0.9	9.0 ± 1.6
12	349	15 December 2011	14.1 ± 6.4	8.2 ± 2.1	3.9 ± 0.9	8.4 ± 3.0
13	350	16 December 2011	12.2 ± 3.2	5.6 ± 1.5	6.1 ± 0.9	7.9 ± 1.8
14	351	17 December 2011	10.2 ± 4.0	5.3 ± 2.2	4.1 ± 0.9	8.1 ± 2.7
15	351	17 December 2011	5.9 ± 3.9	6.1 ± 4.3	4.1 ± 1.3	10.6 ± 4.5
16	364	30 December 2011	8.5 ± 4.1	7.9 ± 1.7	2.2 ± 0.5	9.8 ± 3.0

[a]Silicon abundance is assumed to be constant at 25.7%. Errors are one-standard-deviation fitting errors.

surrounding areas, this difference does not hold everywhere within the NVP. The footprints of two solar-flare-induced XRF events on 15–16 September 2011 correspond well to the location of the 20 May 2011 electron event, and another solar-induced XRF footprint on 13 September 2011 matches that for the 10 November 2011 electron event (see Figure 8). As shown in Table 4, the solar flare measurements of 15–16 September 2011 display lower Mg abundances, characteristic of the NVP. In contrast, the Mg abundance inferred from the flare on 13 September is higher, more in line with the mean value for the surrounding intercrater plains and heavily cratered terrain material (Weider et al., submitted manuscript, 2012). The 15 September 2011 flare footprint overlaps that of the 20 May 2011 electron event, and its Mg value of 7.2 ± 1.1 wt% is in good agreement with the value of 6.3 ± 1.1 wt% for Mg modeled for the 20 May electron event. The Mg abundance inferred from the 16 September 2011 flare is somewhat higher, at 10.2 ± 1.4 wt%. The Al abundances reported here for the May 20 and November 10 events are also in good agreement with the results of Weider et al. (submitted manuscript, 2012). Abundances for S and Ca modeled for the two electron events are consistent with the B02 values. Also, as indicated in Table 4, the abundances for these same two elements inferred from the three flare events are the same within statistics. But the B02 S and Ca abundance values are higher than those for the flare events.

[26] As indicated in Table 3, most of the electron-induced fluorescence events match the B02 values for Al, but several appear consistent with a lower value of ∼5–6 wt%. One such event on 13 August 2011 (number 5) is displayed in Figure 9. The difference in the Al modeled abundance is evident in the model fit to the spectrum from the Al-filtered detector, whereas little difference is seen between the two models in Figure 9 for the Mg-filtered detector or the unfiltered detector.

[27] Si was not varied in any of the model fits and was held at the B02 value of 25.7 wt%. The Si composition is not expected to vary markedly over the planet [*Peplowski et al.*, 2012], and the adopted value is consistent with that found by N11.

5.2. Sulfur

[28] One of the unexpected results from the solar-induced XRF results (N11) is the high abundance of sulfur found on Mercury's surface, in the range ∼1–4 wt%. This unusually high abundance for S, usually considered a volatile element, is an order of magnitude higher than that of lunar and terrestrial basalts. The spectra from electron-induced fluorescence show similarly high S content. In Figure 10, spectra from the electron events from 13 August 2011 (number 5) and from 30 December 2011 (number 16) are compared with that for the B02 model, but with S abundance in the latter allowed to vary. A higher value of ∼6 wt% best matches the 13 August measurements. The 30 December measurements are more consistent with a somewhat lower value of ∼2 wt%.

[29] The S values obtained from the electron events are typically higher than those from the solar flare events. The S abundance from B02 gives a S/Si ratio of ∼0.16, which is at the very top end of the distribution from the solar flare data, and more than a factor of 2 higher than the mean value, ∼0.06 (Weider et al., submitted manuscript, 2012).

5.3. Calcium

[30] Fourteen of the 16 events in Table 3 are consistent with the B02 value for Ca of 8.4 wt%. The Ca abundance of B02 corresponds to a Ca/Si ratio of 0.32, about 50% higher than the average ratio derived by N11. Some of the flares in N11 gave ratios of ∼0.3, so the difference may simply reflect spatial heterogeneity on Mercury's surface. However, it may also reflect a systematic error in either or both of the data sets. This possibility will be discussed in more detail below.

[31] Spectra from one of the low-Ca events, detected on 10 December 2011 (number 9), are compared with model spectra corresponding to ∼8.4 and 4.4 wt% Ca in Figure 11. The data clearly favor the low-Ca interpretation.

5.4. Titanium and Iron

[32] The Ti and Fe abundances in the B02 model are small: 0.12 wt% and 0.19 wt%, respectively. The electron-induced X-ray emission measurements presented here appear to support these low values. There is little evidence for the fluorescent lines from either of these elements in any

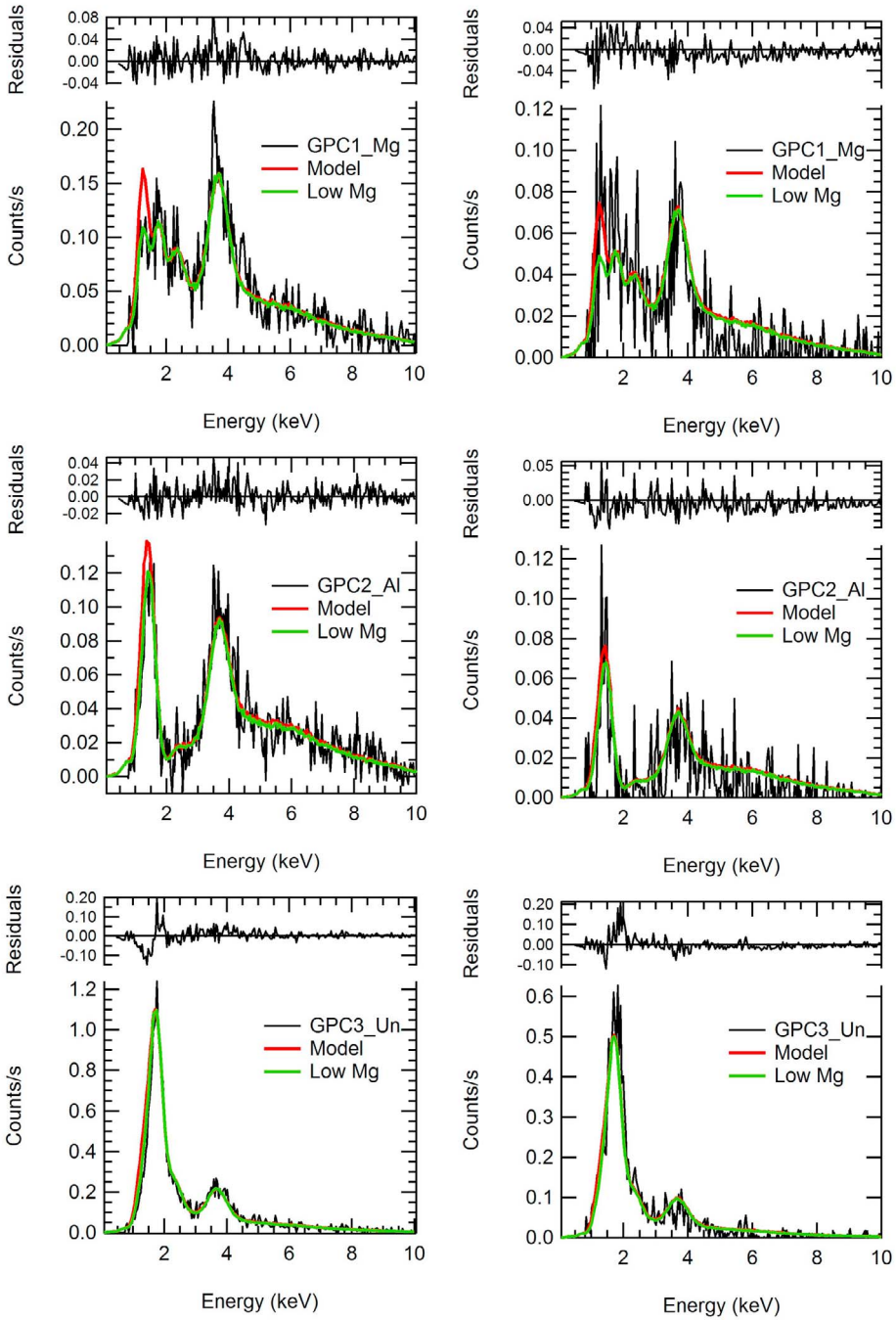

Figure 7. Two models fit to spectra from events on (left) 20 May 2011 (number 3) and (right) 10 November 2011 (number 8) with different Mg abundances. The standard Mg value of 11.5 wt% is indicated by the red line; the green line is for a lower Mg value of 6.3 wt%. Residuals are for the low-Mg model.

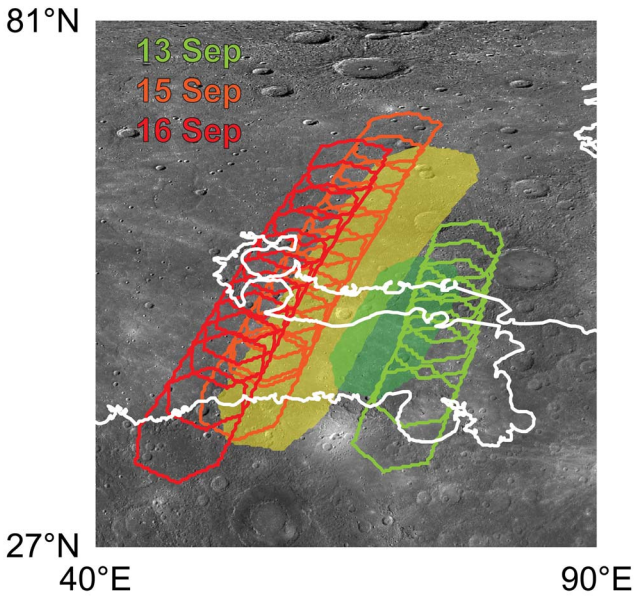

Figure 8. Area around footprints 3 and 8 from Figure 3 (shown in solid yellow and green, respectively). Also shown are footprints from solar flare XRS spectra (open shapes) analyzed by Weider et al. (submitted manuscript, 2012) that overlap those of the electron-induced X-ray emission analyses in this paper. The footprints for the 13 September 2011 flare event are in green, those for the 15 September 2011 flare event are in orange, and those for the 16 September 2011 flare event are in red. The elemental abundances derived from the separate analyses are compared in Table 4.

of the individual spectra, though upper limits may be obtained, as described below. From N11, analysis of several of the larger flares gave Fe abundances in the range 1–3 wt%. All Ti values reported were less than 1 wt%.

[33] To improve statistics, the three GPC spectra for the 11 December 2011 event (number 10) are summed in Figure 12, allowing a more detailed examination of the portion of the spectrum at energies above 4 keV. The summed spectrum is compared with those from three different models (also summed for the three GPCs) across which the Ti and Fe abundances vary but the B02 composition otherwise applies. Values of 1.0 and 2.0 wt % for both Ti and Fe are shown, as well as the standard B02 model. Abundances for Ti and Fe somewhat higher than the B02 composition are suggested, perhaps as high as 1 wt%, but probably not much higher. None of the other events in the set show evidence of Ti or Fe in any greater abundance than that inferred from the 11 December event.

5.5. Systematic Errors

[34] The penetration depth of ~1–10 keV electrons is much less than that of ~1–10 keV X-rays; only a few μm for the electrons, but several tens of μm for the X-rays. Any heterogeneity at this level, perhaps due to space weathering, might be responsible for some of the differences observed with the two measurement techniques.

[35] Both the S and Ca abundances reported here are higher than those reported by Weider et al. (submitted manuscript, 2012), but the Ca/S ratios are consistent. The average value for the Ca/S ratio from this work is 1.95 ± 0.7; from the solar flare measurements, the ratio is 2.35 ± 0.8. Systematic uncertainties that preferentially affect the higher end of the electron spectrum may provide at least a partial explanation, as discussed below.

[36] The largest source of systematic error in these measurements is the uncertainty in the electron excitation spectrum. We have assumed that the spectrum modeled by *Ho et al.* [2011a] is that of the electrons that impact the surface. Modeling largely supports this assumption, but small changes can affect the inferred abundances. Below we consider for two events how variations in the excitation spectrum may affect inferred compositional values.

5.5.1. Event 5, 13 August 2011

[37] An indication of how changes in the assumed excitation spectrum can affect the model result is shown in Figure 13. Plots of four different excitation spectra, all based on the kappa function, are shown in Figure 14. The kappa function, described in *Christon* [1987], is given by $j \sim [E/E_o][1 + E/KE_o]^{-K-1}$, where E_o and K are the modal energy and kappa, respectively. Kappa is held constant across the four excitation spectra, but E_o is varied: E_o = 1.0 for M2-E2, E_o = 0.8 for kappa-1, E_o = 1.2 for kappa-2, and E_o = 1.4 for kappa-3.

[38] The impact of increasing the modal energy is effectively to harden the electron excitation spectrum, thus increasing the emission at higher energies, as discussed below. For example, integrating the flux from 8 to 10 keV

Table 4. Comparison of Elemental Abundance Estimates (for Mg, Al, S, and Ca) Derived From Electron-Induced X-Ray Emission (This Work) and Solar-Induced XRF Analyses (Weider et al., submitted manuscript, 2012)

	10 November 2011 (Electron-Induced)	13 September 2011 (XRF)	20 May 2011 (Electron-Induced)	15 September 2011 (XRF)	16 September 2011 (XRF)	15 and 16 September 2011 (XRF)
Mg	11.0 ± 3.8	12.0 ± 2.3	6.3 ± 1.1	7.2 ± 1.1	10.2 ± 1.4	8.6 ± 2.0
Al	6.4 ± 1.9	6.0 ± 1.5	5.8 ± 0.9	6.8 ± 0.7	7.3 ± 1.6	7.1 ± 1.2
S	4.5 ± 0.9	1.1 ± 0.4	3.9 ± 0.4	1.5 ± 0.2	1.0 ± 0.2	1.3 ± 0.3
Ca	6.7 ± 2.7	3.8 ± 0.4	9.5 ± 1.6	4.2 ± 0.3	3.5 ± 0.5	3.9 ± 0.6

[a]Note: For the 13 September 2011 solar flare the set of surface footprints overlaps the footprint of the 10 November 2011 electron event (see Figure 8). The surface footprints of solar flares on 15 and 16 September 2011 overlap that of the 20 May 2011 electron event.

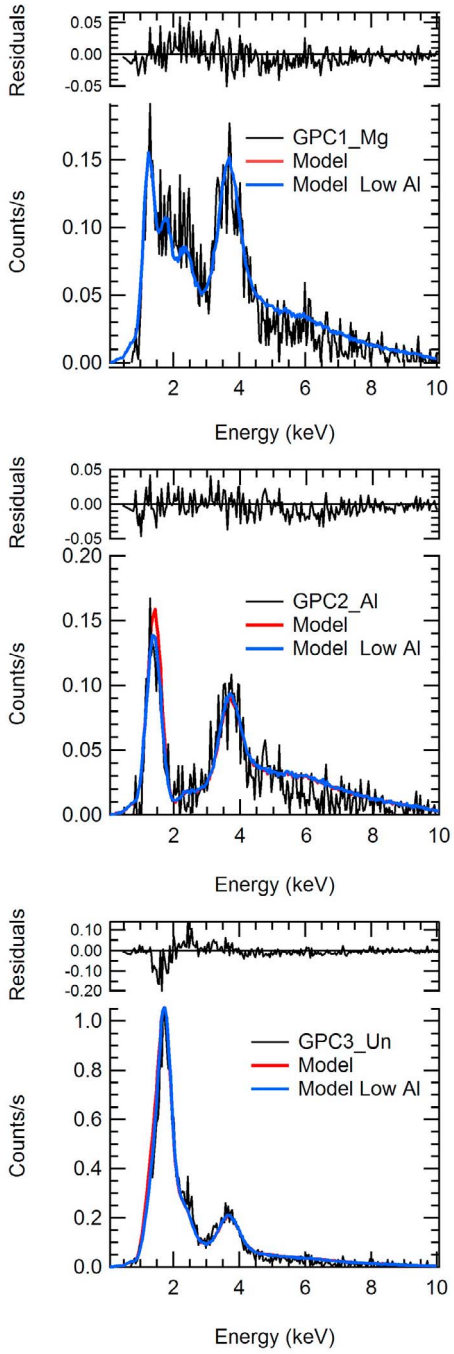

Figure 9. Models fit to spectra from the 13 August 2011 event (number 5) with different Al abundances. The model using the standard B02 value (7.15%) is indicated in red, and a model with a lower Al value of 5 wt% is shown in blue. The residuals are for the low-Al model.

and comparing this result to the integral from 1 to 3 keV gives ratios of 0.025, 0.047, 0.077, and 0.115 for the kappa-1, M2-E2, kappa-2, and kappa-3 curves, respectively.

[39] Spectra for three different excitation models, M2-E2, kappa-1, and kappa-2, are compared with the observed spectra for the 13 August 2011 (No. 5) event. The largest differences are seen at higher energies. The continuum above the Ca line varies markedly. The size of the modeled Ca line itself varies by ~35% in the three detectors. However, changes in E_o have relatively little impact on the lower-energy portion of the model spectra. For the Mg, Al, Si, and S lines, changes are ~10% or less. We may therefore conclude that, although systematic uncertainties may alter values for the Ca line by as much as ~30%, for the elements of lower atomic number the errors due to uncertainties in the excitation spectrum appear to be no more than ~10%.

5.5.2. Event 7, 4 November 2011

[40] Spectra for three different excitation models (M2-E2, kappa-2, and kappa-3) are compared with the observed spectra for the 4 November 2011 event in Figure 15 (left). This event deviates from the standard model more than any of the other events in the sample set. The M2-E2 excitation spectrum and standard B02 composition underpredict the size of the Ca line by ~43%. Large differences at the higher energies and relatively smaller differences at lower energies are again observed. The kappa-3 model case matches the observed Ca line fairly well with the standard B02 composition, but it overpredicts the signal for the Mg, Al, and S lines. Figure 15 (right) compares the kappa-3 model with a variation of B02 that reduces Mg by ~30%, Al by ~30%, and S by ~50%. The 4 November 2011 event appears to support these lower values for Mg, Al, and S, but systematic errors due to uncertainties in the excitation spectrum make it less likely that the Ca abundance is very different from that of B02.

5.6. Background

5.6.1. Galactic Cosmic Rays

[41] The background in the GPCs is primarily due to interactions of galactic cosmic rays with the detector gas. The shape of this background is fairly constant, except during solar particle events. Background subtraction is accomplished by identifying an extended time period near an electron event with no fluorescent X-ray or other non-GCR components. Background spectra are summed over several hours and exceed the length of an electron event by at least an order of magnitude to minimize statistical errors. Background spectra are time normalized to event spectra. Figure 16 shows spectra for the second event on 13 August 2011 (number 6) without background subtraction compared with the time normalized background. In this case, the event spectra are 280 s in duration, whereas the background is summed over a time period of 23,100 s. Background count rates in the three GPCs are similar. Over this time period of more than 6 h, the background never deviated from the mean by more than ~3% for any of the detectors. Systematic uncertainty from GCR background subtraction should not exceed ~10%.

5.6.2. Fluorescence in the Filters

[42] It is possible that the thin filters on two of the GPCs may absorb X-rays, producing the K-alpha fluorescence lines from Mg and Al in the filters themselves, thereby adding to the signal detected by the filtered GPCs. However, this effect is included in the GPC model response, so both model and measurement contain this background component. Additionally, *Nittler et al.* [2001] examined this effect for the XRS on the NEAR mission and found the filter enhancement effect to be small, less than ~10% of the

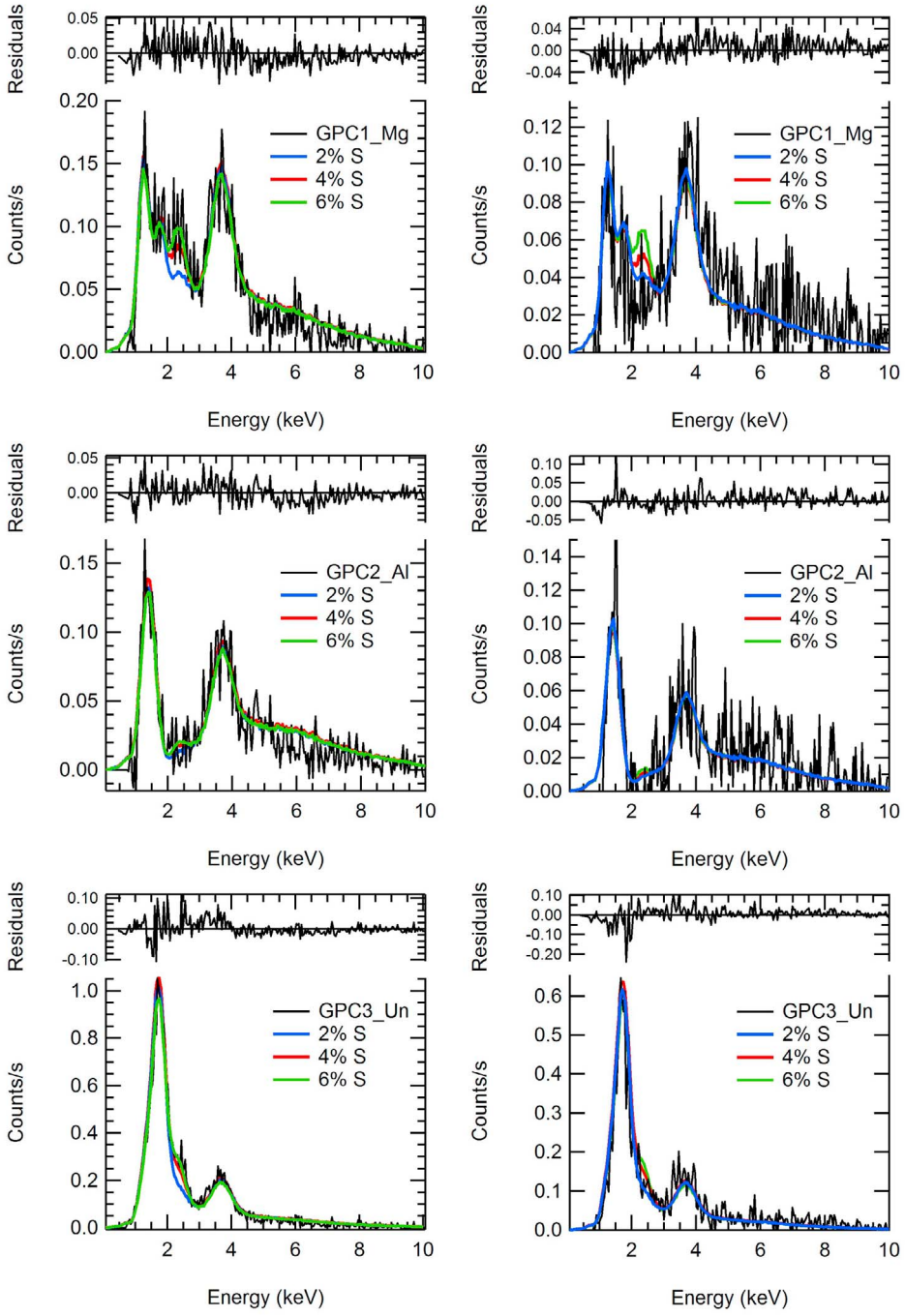

Figure 10. Models fit to spectra from the events of (left) 13 August 2011 (number 5) and (right) 30 December 2011 (number 16) with different S abundances: 2 wt% S (blue line), 4 wt% S (red line), and 6 wt% S (green line). For the 13 August event, the residuals are for the model with 6 wt% S, and for the 30 December event the residuals are for the model with 2 wt% S.

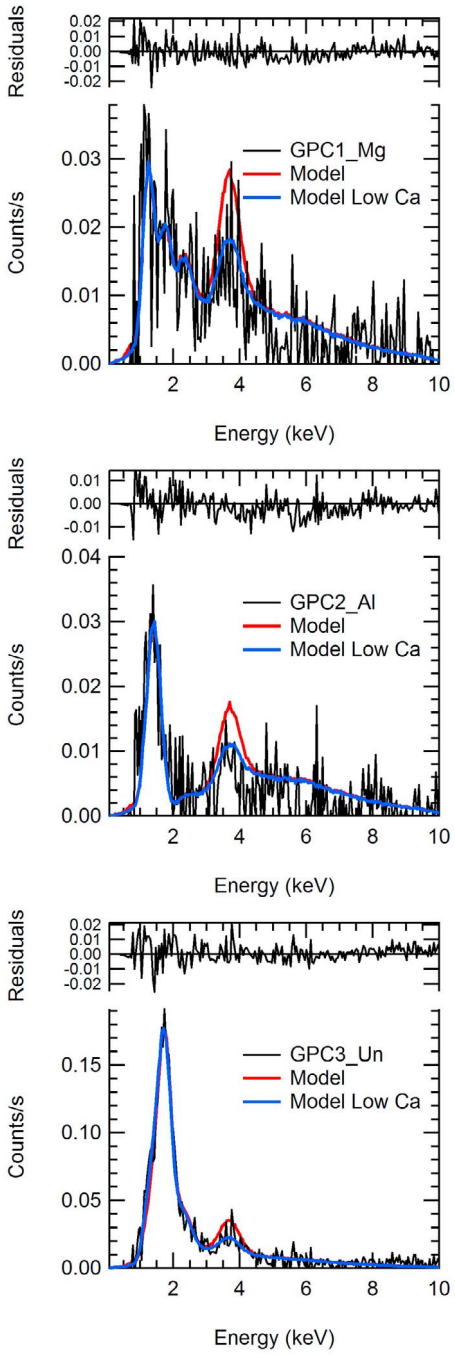

Figure 11. Models fit to the spectra of the three GPCs for the event of 10 December 2011 (number 9) with different Ca abundances. The model with the standard B02 value for Ca (8.4%) is indicated in red, and a model with a lower value of 4.4 wt% Ca is shown in blue. The residuals are for the low-Ca model.

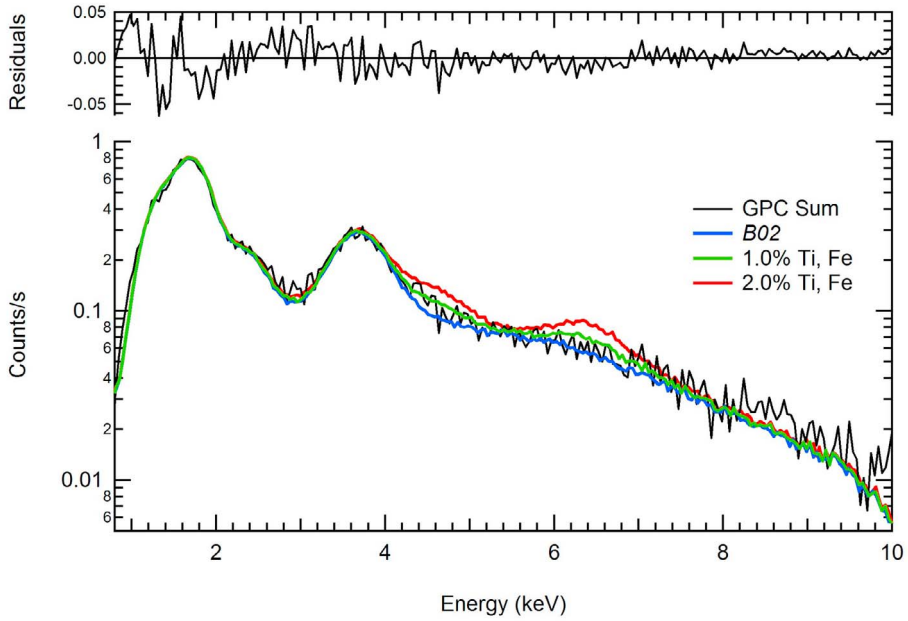

Figure 12. Models fit to summed GPC spectra for the event of 11 December 2011 (number 10) with different Ti and Fe abundances. The blue line is the standard model of B02 with 0.12 wt % Ti and 0.19 wt% Fe. The green and red lines represent 1.0 and 2.0 wt%, respectively, for both Ti and Fe. The residuals are for the model with 1.0 wt% Ti and Fe.

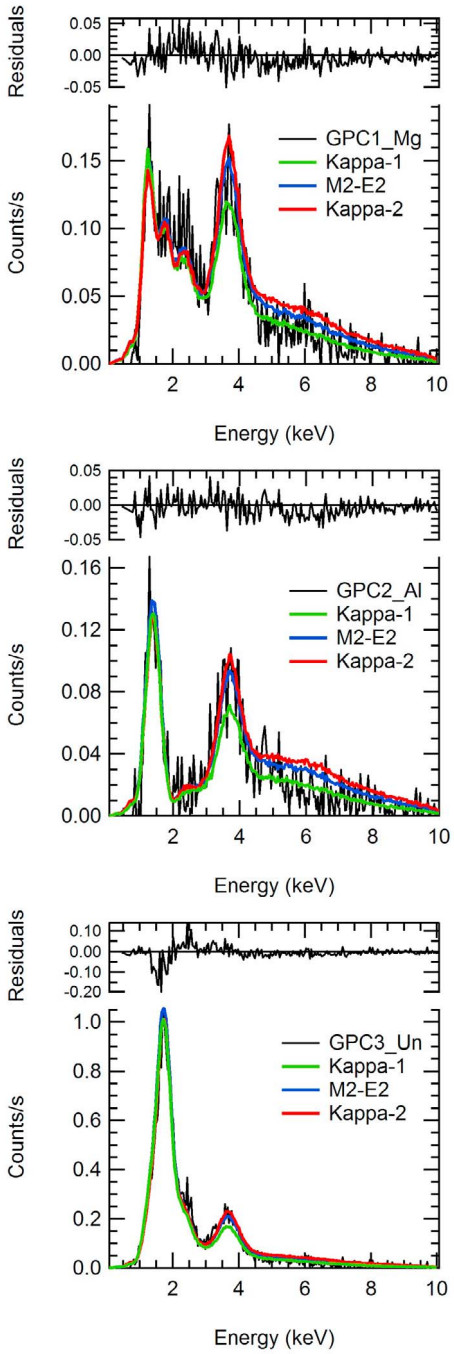

Figure 13. Models fit to the event of 13 August 2011 (number 5) with different values for the modal energy, E_o. The blue curve is the standard M2-E2 excitation spectrum, kappa-1 is in green, and kappa-2 is in red. Residuals are for the M2-E2 model.

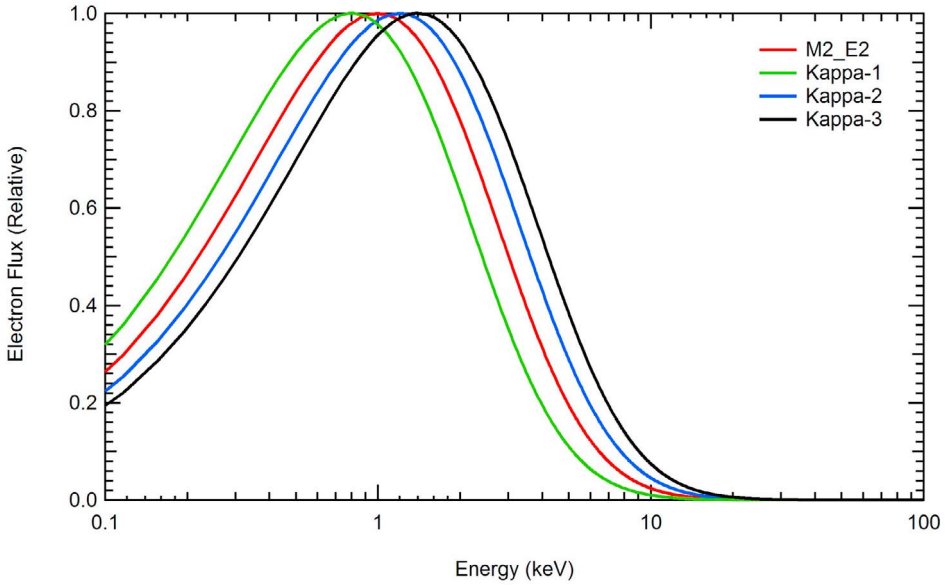

Figure 14. Plots of four different kappa-function electron spectra. Kappa is held constant across the models, but E_o is varied: M2-E2 (E_o = 1.0) is in red, kappa-1 (E_o = 0.8) is in green, kappa-2 (E_o = 1.2) is in blue, and kappa-3 (E_o = 1.4) is in black.

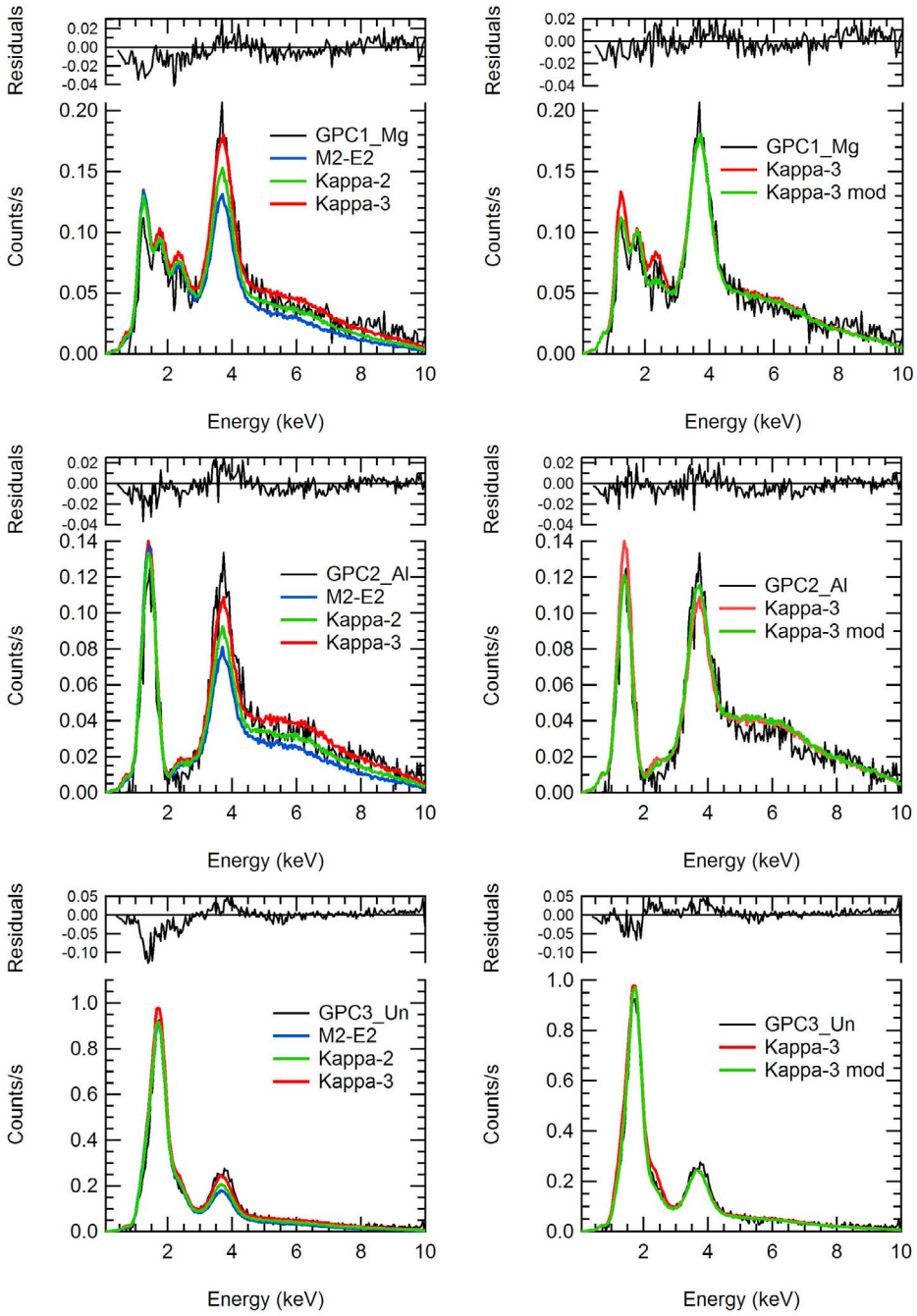

Figure 15. (left) Models fit to spectra from the event of 4 November 2011 (number 7) with different values for the modal energy, E_o. The blue curve is the standard M2-E2 excitation spectrum, kappa-2 is in green, and kappa-3 is in red. (right) The kappa-3 excitation spectrum is used for both the standard B02 composition (red curve) and for a composition with Mg, Al, and S values reduced as described in the text (green curve). Residuals for the kappa-3 electron distribution are shown on the left. Residuals for the modified kappa-3 electron distribution are shown on the right.

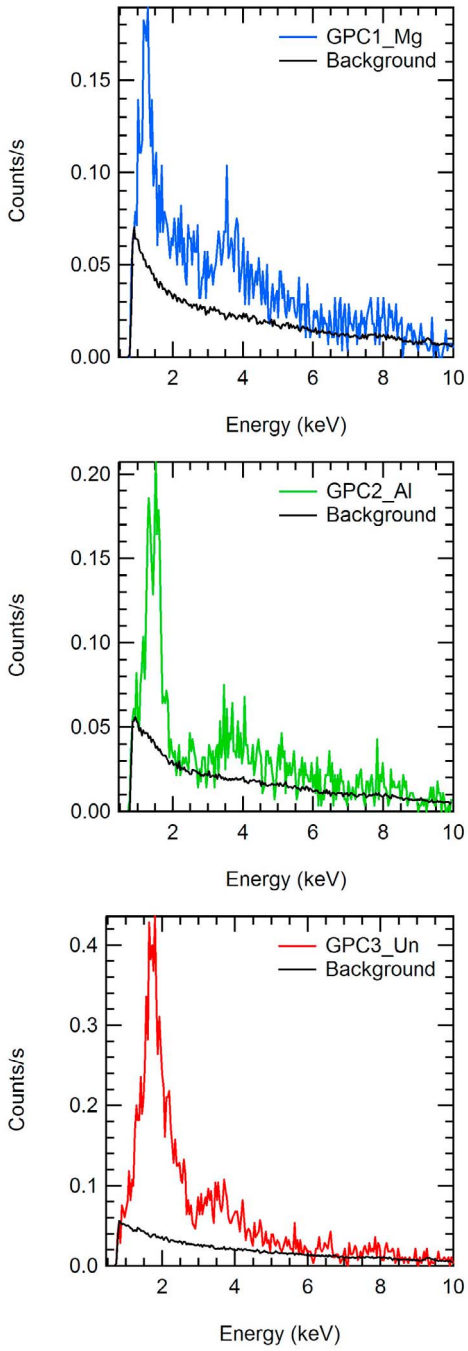

Figure 16. GPC spectra for the second event on 13 August 2011 (number 6). Mg-filtered (blue), Al-filtered (green), and red (unfiltered) GPC spectra are shown with no background subtraction. Corresponding time-normalized background spectra are shown in black. The event duration is 280 s. Background spectra were collected over a period of 23,100 s.

detector signal. The filters on the MESSENGER GPCs are thinner than those used on NEAR, and the Mercury Al abundance is higher than that of Eros. Both factors further reduce the size of this effect.

5.6.3. Quiet Sun

[43] We generally excluded events detected on the dayside to avoid a quiet-Sun component in the measurement, which would require an additional background correction. Of the 16 events included in this work, 14 were on the nightside and two on the dayside. The two on the dayside were the events on 3 May 2011 (number 1) and 6 May 2011 (number 2). Event number 2 showed no contribution from the quiet Sun, so no correction was necessary. Event number 1 did exhibit a quiet-Sun component, which was corrected by subtracting a time-normalized quiet-Sun measurement that had similar solar spectrum (within 10% for both temperature and intensity) and incidence and emission angles. The relatively large uncertainties for this event seen in Table 3, especially for Mg and Al, are in large part due to this additional correction not required for any of the other events.

6. Summary

[44] All 16 electron events included in this work show clear evidence of fluorescence for X-ray energies up to the Ca line. The agreement seen in Figure 2 between the XRS modeled spectrum from *Ho et al.* [2011a] at energies above 35 keV and a typical EPS electron measurement helps to confirm the XRS modeling. Also, the modeled XRS electron spectrum with a mean value near 1 keV, as seen in Figure 14, is supported by the global electron transport simulations of *Schriver et al.* [2011a]. Reasonable correspondence is found between the locations of XRS fluorescence events and model predictions for the nightside locations of the precipitation of ~1 keV electrons from about midnight to morning, as indicated in Figure 5.

[45] Ten of the 16 events listed in Tables 1 and 3 were highlighted in this paper, because they generally had better count statistics, thus making comparison to the models more meaningful. It is also worth noting that event count rates do not correlate with integration times. For example, events on 10 and 11 December 2011 (numbers 9 and 10) had nearly the same integration time, but the count rate for the 11 December event was more than three times that for the 10 December event. Similarly, the two 13 August events had comparable integration times, but the earlier event (number 5) had twice the count rate of the later event (No. 6). This difference is most likely due to the variable electron flux. We know from *Ho et al.* [2011a] that the flux of electrons striking the GPCs varied by more than an order of magnitude. Similar variations in count rate have been observed for these events since MESSENGER entered into orbit about Mercury. It seems probable that the flux of electrons impacting the surface varies in a similar manner.

[46] The surface elemental compositions derived from these measurements are in line, to within expected uncertainties, with those derived from solar-induced XRF by N11 and Weider et al. (submitted manuscript, 2012), confirming the value of electron-induced X-ray emission measurements for geochemical analysis at Mercury. There is clear evidence for spatial variation in Mg, Al, and S across Mercury's surface. Ca may also vary, but systematic uncertainties in the input spectrum may have a substantial impact on inferred Ca abundances.

[47] **Acknowledgments.** The authors thank the MESSENGER team for the development, cruise, orbit insertion, and Mercury orbital operations of the MESSENGER spacecraft. This work was supported in part by the National Aeronautics and Space Administration's Discovery Program through grant number NNX07AR59G to the Catholic University of America. The MESSENGER project is supported under NASA contracts NAS5-97271 to The Johns Hopkins University Applied Physics Laboratory and NASW-00002 to the Carnegie Institution of Washington. Global simulation particle modeling was supported by the NASA MESSENGER Participating Scientist grant NNX07AR62G and NASA Geospace grant NNX12AD08G. Resources supporting the XRS analysis and the global simulations were provided by the NASA High-End Computing (HEC) Program through the NASA Center for Computational Sciences (NCCS) at Goddard Space Flight Center and NASA Advanced Supercomputing (NAS) at Ames Research Center.

References

Adler, I., and J. I. Trombka (1977), Orbital chemistry-lunar surface analysis from X-ray and gamma-ray remote sensing experiments, *Phys. Chem. Earth*, *10*, 17–43, doi:10.1016/0079-1946(77)90004-0.

Adler, I., et al. (1972a), Apollo 15 geochemical X-ray fluorescence experiment: Preliminary report, *Science*, *175*, 436–440, doi:10.1126/science.175.4020.436.

Adler, I., et al. (1972b), Apollo 16 geochemical X-ray fluorescence experiment: Preliminary report, *Science*, *177*, 256–259, doi:10.1126/science.177.4045.256.

Adler, I., et al. (1973), Apollo 15 and 16 results of the integrated geochemical experiment, *Moon*, *7*, 487–504, doi:10.1007/BF00564649.

Anderson, B. J., C. L. Johnson, H. Korth, M. E. Purucker, R. M. Winslow, J. A. Slavin, S. C. Solomon, R. L. McNutt Jr., J. M. Raines, and T. H. Zurbuchen (2011), The global magnetic field of Mercury from MESSENGER orbital observations, *Science*, *333*, 1859–1862, doi:10.1126/science.1211001.

Bhardwaj, A., et al. (2007), X-rays from solar system objects, *Planet. Space Sci.*, *55*, 1135–1189, doi:10.1016/j.pss.2006.11.009.

Burbine, T. H., T. J. McCoy, L. R. Nittler, G. K. Benedix, E. A. Cloutis, and T. L. Dickinson (2002), Spectra of extremely reduced assemblages: Implications for Mercury, *Meteorit. Planet. Sci.*, *37*, 1233–1244, doi:10.1111/j.1945-5100.2002.tb00892.x.

Burbine, T. H., J. I. Trombka, P. M. Bergstrom Jr., and S. P. Christon (2005), Calculating the X-ray fluorescence from the planet Mercury due to high energy electrons, *Lunar Planet. Sci.*, *XXXVI*, Abstract 1416.

Christon, S. P. (1987), A comparison of the Mercury and Earth magnetospheres: Electron measurements and substorm time scales, *Icarus*, *71*, 448–471, doi:10.1016/0019-1035(87)90040-6.

Cravens, T. E., and A. N. Maurellis (2001), X-ray emission from scattering and fluorescence of solar X-rays at Venus and Mars, *Geophys. Res. Lett.*, *28*, 3043–3046, doi:10.1029/2001GL013021.

Fink, H. H., J. H. M. M. Schmitt, and F. R. Harden Jr. (1988), The scattered solar X-ray background in low Earth orbit, *Astron. Astrophys.*, *193*, 345–356.

Goldstein, J., D. E. Newbury, D. C. Joy, C. E. Lyman, P. Echlin, E. Lifshin, L. Sawyer, and J. R. Michael (2003), *Scanning Electron Microscopy and X-Ray Microanalysis*, 3rd ed., 586 pp., Springer, New York, doi:10.1007/978-1-4615-0215-9.

Head, J. W., et al. (2011), Flood volcanism in the northern high latitudes of Mercury revealed by MESSENGER, *Science*, *333*, 1853–1856, doi:10.1126/science.1211997.

Ho, G. C., R. D. Starr, R. E. Gold, S. M. Krimigis, J. A. Slavin, D. N. Baker, B. J. Anderson, R. L. McNutt Jr., L. R. Nittler, and S. C. Solomon (2011a), Observations of suprathermal electrons in Mercury's magnetosphere during the three MESSENGER flybys, *Planet. Space Sci.*, *59*, 2016–2025, doi:10.1016/j.pss.2011.01.011.

Ho, G. C., et al. (2011b), MESSENGER observations of transient bursts of energetic electrons in Mercury's magnetosphere, *Science*, *333*, 1865–1868, doi:10.1126/science.1211141.

Korth, H., B. J. Anderson, J. M. Raines, J. A. Slavin, T. H. Zurbuchen, C. L. Johnson, M. E. Purucker, R. M. Winslow, S. C. Solomon, and R. L. McNutt Jr. (2011), Plasma pressure in Mercury's equatorial magnetosphere derived from MESSENGER Magnetometer observations, *Geophys. Res. Lett.*, *38*, L22201, doi:10.1029/2011GL049451.

Lisse, C. M., et al. (1996), Discovery of X–ray and extreme ultraviolet emission from Comet C/Hyakutake 1996 B2, *Science*, *274*, 205–209, doi:10.1126/science.274.5285.205.

Metzger, A. E., D. A. Gilman, J. L. Luthey, K. C. Hurley, H. W. Schnopper, F. D. Seward, and J. Sullivan (1983), The detection of X-rays from Jupiter, *J. Geophys. Res.*, *88*, 7731–7741, doi:10.1029/JA088iA10p07731.

Narendranath, S., et al. (2011), Lunar X-ray fluorescence observations by the Chandrayaan-1 X-ray Spectrometer (C1XS): Results from the nearside southern highlands, *Icarus*, *214*, 53–66, doi:10.1016/j.icarus.2011.04.010.

Nittler, L. R., et al. (2001), X-Ray fluorescence measurements of the surface elemental composition of asteroid 433 Eros, *Meteorit. Planet. Sci.*, *36*, 1673–1695, doi:10.1111/j.1945-5100.2001.tb01856.x.

Nittler, L. R., et al. (2011), The major-element composition of Mercury's surface from MESSENGER X-ray spectrometry, *Science*, *333*, 1847–1850, doi:10.1126/science.1211567.

Okada, T., K. Shirai, Y. Yamamoto, T. Arai, K. Ogawa, K. Hosono, and M. Kato (2006), X-ray fluorescence spectrometry of asteroid Itokawa by Hayabusa, *Science*, *312*, 1338–1341, doi:10.1126/science.1125731.

Okada, T., et al. (2010), X-ray fluorescence spectrometry of lunar surface by XRS onboard SELENE (Kaguya), *Trans. Space Technol. Jpn.*, *7*, Tk_39–Tk_42.

Pelowitz, D. B. (Ed.) (2005), MCNPX User's Manual, version 2.5.0, *Rep. LA-UR-94–1817*, 473 pp., Los Alamos Natl. Lab., Los Alamos, N. M.

Peplowski, P. N., et al. (2012), Variations in the abundances of potassium and thorium on the surface of Mercury: Results from the MESSENGER Gamma-Ray Spectrometer, *J. Geophys. Res.*, doi:10.1029/2012JE004141, in press.

Russell, C. T., D. N. Baker, and J. A. Slavin (1988), The magnetosphere of Mercury, in *Mercury*, edited by F. Vilas, C. R. Chapman, and M. S. Matthews, pp. 514–561, Univ. of Ariz. Press, Tucson.

Schlemm, C. E., II, et al. (2007), The X-Ray Spectrometer on the MESSENGER spacecraft, *Space Sci. Rev.*, *131*, 393–415, doi:10.1007/s11214-007-9248-5.

Schriver, D., et al. (2011a), Electron transport and precipitation at Mercury during the MESSENGER flybys: Implications for electron-stimulated desorption, *Planet. Space Sci.*, *59*, 2026–2036, doi:10.1016/j.pss.2011.03.008.

Schriver, D., et al. (2011b), Quasi-trapped ion and electron populations at Mercury, *Geophys. Res. Lett.*, *38*, L23103, doi:10.1029/2011GL049629.

Simpson, J. A., J. H. Eraker, J. E. Lamport, and P. H. Walpole (1974), Electrons and protons accelerated in Mercury's magnetic field, *Science*, *185*, 160–166, doi:10.1126/science.185.4146.160.

Solomon, S. C., et al. (2001), The MESSENGER mission to Mercury: Scientific objectives and implementation, *Planet. Space Sci.*, *49*, 1445–1465, doi:10.1016/S0032-0633(01)00085-X.

Starr, R., et al. (2000), Instrument calibrations and data analysis procedures for the NEAR X-ray spectrometer, *Icarus*, *147*, 498–519, doi:10.1006/icar.2000.6453.

Trávníček, P. M., D. Schriver, P. Hellinger, D. Hercik, B. J. Anderson, M. Sarantos, and J. A. Slavin (2010), Mercury's magnetosphere-solar wind interaction for northward and southward interplanetary magnetic field: Hybrid simulation results, *Icarus*, *209*, 11–22, doi:10.1016/j.icarus.2010.01.008.

Trombka, J. I., et al. (2000), The elemental composition of asteroid 433 Eros: Results of the NEAR-Shoemaker X-ray spectrometer, *Science*, *289*, 2101–2105, doi:10.1126/science.289.5487.2101.

Weider, S. Z., et al. (2012), The Chandrayaan-1 X-ray spectrometer: First results, *Planet. Space Sci.*, *60*, 217–228, doi:10.1016/j.pss.2011.08.014.

Wurz, P., and L. Blomberg (2001), Particle populations in Mercury's magnetosphere, *Planet. Space Sci.*, *49*, 1643–1653, doi:10.1016/S0032-0633(01)00102-7.

Zurbuchen, T. H., et al. (2011), MESSENGER observations of the spatial distribution of planetary ions near Mercury, *Science*, *333*, 1862–1865, doi:10.1126/science.1211302.